32-year record-high surface melt in 2019/2020 on north George VI Ice Shelf, Antarctic Peninsula

Alison F. Banwell[1,2], Rajashree Tri Datta[3,4], Rebecca L. Dell[2], Mahsa Moussavi[5,1], Ludovic Brucker[3,6],
5   Ghislain Picard[7], Christopher A. Shuman[3,8] Laura A. Stevens[9,10]

1)   Cooperative Institute for Research in Environmental Sciences (CIRES), University of Colorado, Boulder, CO, USA
2)   Scott Polar Research Institute (SPRI), University of Cambridge, Cambridge, UK
3)   Cryospheric Sciences Laboratory, NASA Goddard Space Flight Center, Greenbelt, MD, USA l
4)   Earth System Science Interdisciplinary Center, University of Maryland, College Park, MD, USA
10 5)   National Snow and Ice Data Center (NSIDC), University of Colorado Boulder, CO 80309, USA
6)   Goddard Earth Sciences Technology and Research Studies and Investigations, Universities Space Research Association, Columbia, MD, USA
7)   Univ. Grenoble Alpes, CNRS, Institut des Géosciences de l'Environnement (IGE), UMR 5001, 38041 Grenoble, France
8)   Joint Center for Earth Systems Technology, University of Maryland, Baltimore County, Greenbelt, MD, USA
15 9)   Department of Earth Sciences, University of Oxford, Oxford, UK
10) Lamont-Doherty Earth Observatory of Columbia University, Palisades, NY, USA

Correspondence to: Alison F Banwell (alison.banwell@colorado.edu)

Abstract In the 2019/2020 austral summer, the surface melt duration and extent on the northern George VI Ice Shelf (GVIIS)
was exceptional compared to the 31 previous summers of dramatically lower melt. This finding is based on analysis of near-
20 continuous 41-year satellite microwave radiometer (and scatterometer) data, which are sensitive to meltwater on the ice-shelf
surface and in the near-surface snow. Using optical satellite imagery from Landsat 8 (since 2013) and Sentinel-2 (since 2017),
record volumes of surface meltwater ponding are also observed on north GVIIS in 2019/2020, with 23% of the surface area
covered by 0.62 km^3 of meltwater on January 19. These exceptional melt and surface ponding conditions in 2019/2020 were
driven by sustained air temperatures ≥ 0°C for anomalously long periods (55–90 hours) from late November onwards, likely
25 driven by warmer northwesterly and northeasterly low-speed winds. Increased surface ponding on ice shelves may threaten
their stability through increased potential for hydrofracture initiation; a risk that may increase due to firn air content depletion
in response to near-surface melting.

1. Introduction

30 Since the 1950s, the Antarctic Peninsula (AP) (Fig. 1a) has experienced faster increases in ocean and atmospheric warming
than the rest of the Antarctic Ice Sheet (Siegert et al. 2019; Smith et al 2020; Trusel et al. 2015). The rate of mass loss from
the AP is accelerating (Barrand et al., 2013; Shepherd et al., 2018) and has tripled since 1990 (Rignot et al., 2019). Mass loss
is currently focused at marine margins, where the mass balance is controlled by complex interactions between the ice, ocean,

atmosphere and bed conditions (Scambos et al., 2000; Bell et al., 2018; Tuckett et al. 2019; Smith et al., 2020). An important

35 part of this system are ice shelves, which have a total area of ~120,000 km² around the AP (Siegert et al., 2019), and act to buttress the inland ice from flowing into the ocean (Scambos et al. 2004; De Rydt et al., 2015; Fürst et al., 2016; Gudmundsson et al., 2019).

Ice-shelf surface melting, which results in ice-shelf surface lowering, and if sustained, thinning (Paolo et al., 2015), is connected to ice-shelf stability as follows. In warm summers, meltwater produced at the ice-shelf surface is stored in the

40 perennial snowpack ('firn'). Refreezing of this meltwater releases latent heat into the firn, causing additional melting, firn saturation, and firn air content depletion; eventually facilitating meltwater to pond on the ice-shelf surface (Kuipers Munneke et al., 2014; Holland et al., 2011). Extensive surface ponding (Arthur et al 2020; Dell et al., 2020; Kingslake et al., 2017) may threaten ice-shelf stability due to stress variations associated with meltwater movement, ponding and drainage (Scambos et al., 2000, 2003; MacAyeal et al., 2003; Banwell and MacAyeal, 2015; Banwell et al. 2019). These processes may initiate

45 meltwater-induced vertical fracturing ('hydrofracturing') (Van der Veen, 2007; Dunmire et al., 2020; Lai et al. 2020), especially if the ice shelf is already damaged with a high density of crevasses (Lhermitte et al., 2020). The collapse of the Larsen B ice shelf in 2002 is arguably the most famous break-up event due to its rapidity and extent (e.g. Scambos et al., 2013) and may have been driven by the drainage of ~3000 lakes (Banwell et al, 2013, Robel and Banwell, 2019; Leeson at al., 2020). However surface melting has also been implicated in the large-scale collapse events of Prince Gustav and Larsen A ice shelves

50 over just a few days in late January 1995 (Rott et al., 1996; Doake et al., 1998; Glasser et al., 2011; Scambos et al., 2003), and in the partial collapses of the Wilkins, Larsen B, George VI, and Larsen A ice shelves (Scambos et al. 2003, 2009; Cook and Vaughan, 2010).

Occurrences of extreme melt seasons can lead to substantial changes that may potentially impact the mass balance of the AP and consequently global sea level rise. In the austral summer of 2019/2020, a near-record melt event extended across the AP

55 and was accompanied by two record-high instantaneous surface air temperatures measured by automatic weather stations (AWSs); data that are now under review by the World Meteorological Organization (WMO). On February 6, 2020, Argentina's Esperanza research base measured a potential new record of 18.4°C, before being broken again by a measurement of 20.75°C at Argentina's Marambio base on February 9, 2020. This measurement is almost 1°C higher at latitudes that are nearly 2° further south than the previous WMO record-high for the Antarctic (19.8°C), recorded on January 30, 1982, at the British

60 Antarctic Survey (BAS) research station on Signy Island in the subantarctic South Orkney Islands (King et al., 2017). The 2019/2020 melt event over the AP resulted in widespread surface meltwater ponding on ice shelves, low-elevation outlet glaciers and on ice-capped islands observable in optical satellite imagery (Fig. 1a). Out of all AP ice shelves, the largest area of surface meltwater ponding in 2019/2020 was observed on the northern George VI Ice Shelf (GVIIS); the focus of this study (Fig. 1b).
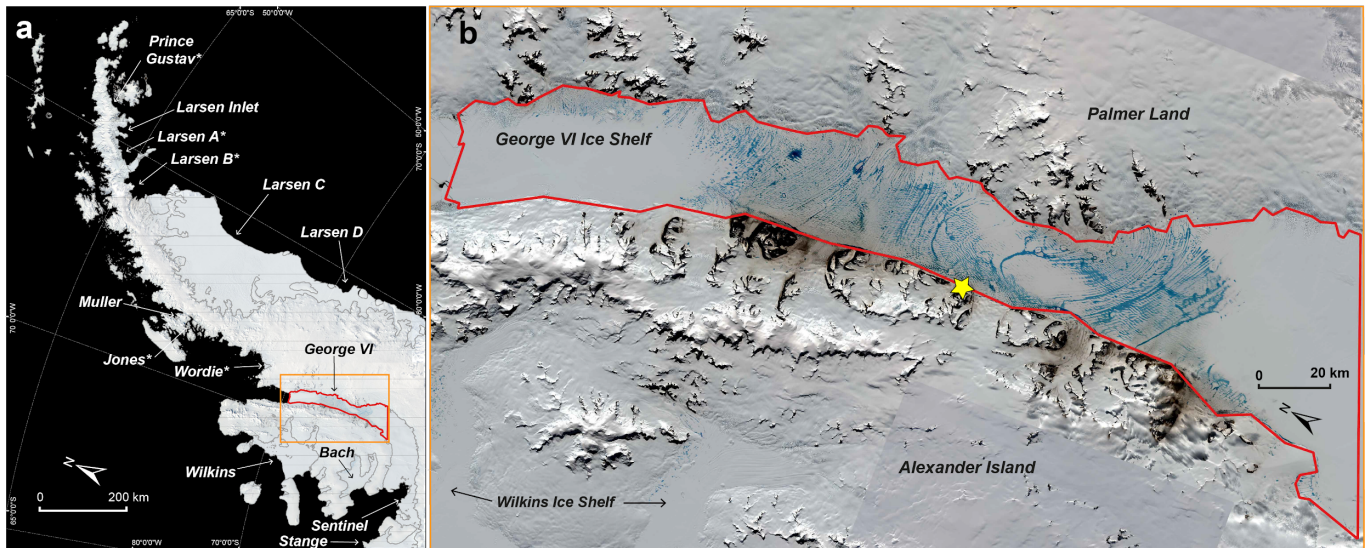
Figure 1. (**a**) Mosaic of cloud-free Moderate Resolution Imaging Spectroradiometer (MODIS) images over the AP, dated from January 19 to February 7, 2020. The MODIS mosaic is sea ice-masked and the ice shelves are delineated with grey lines using the U.S. National Ice Center Operational Antarctic Ice Front and Coastline Data Set 2017-2020 (Readinger, 2020). Ice shelves are labelled with white text; those with * have lost > 50% of their original area since the 1950s (Cook and Vaughan, 2010). The red outline shows the study's Area of Interest (AOI) over north GVIIS. The orange box depicts the area shown in (b). The most extensive area of meltwater ponding is on north GVIIS, however surface meltwater ponding also exists on the northwestern Larsen C Ice Shelf, the northern Wilkins Ice Shelf (also visible in the bottom left corner of b), and on the north and northwest Bach Ice Shelf. (**b**) A mosaic of optical images over the north GVIIS AOI. All images are Sentinel-2 tiles dated January 19, 2020, apart from the two darker tiles (top right and lower right, outside of the AOI) which are Landsat 8 image tiles from January 17 and 19, 2020. The study AOI is delineated by the red outline, and the yellow star shows the location of the Fossil Bluff AWS.

2. Study Site

GVIIS is located in the southwest AP between Alexander Island and Palmer Land (Fig. 1). With an area of ~23,500 km^2 (Rignot et al., 2013), it is the second largest remaining ice shelf on the AP after the Larsen C. GVIIS has two ice fronts, separated by ~450 km along its centreline: a northern ice front that calves into Marguerite Bay, and a southern ice front that terminates into the Ronne Entrance (Holt et al., 2013). GVIIS is structurally complex, with distinct flow units originating in Palmer Land flowing across to, and impinging against, Alexander Island (Davies et al. 2017; Reynolds and Hambrey, 1988; Hambrey et al., 2015, Fig. 1b), resulting in a dominantly compressive flow regime (LaBarbera and MacAyeal, 2011). This complex flow regime controls ice-shelf thickness, which varies from ~100 m at both ice fronts to ~600 m in the centre (Davies et al. 2017; Smith et al., 2007).

The Cryosphere
Discussions
Open Access
EGU

The northern GVIIS (~70º15' W to ~72º00' S) experiences particularly high surface summer melt rates, so winter snowfall rarely lasts through the summer (Holt et al., 2013) and extensive areas of ponded surface water have been observed since at least the early 1940s (Wager, 1972; Reynolds, 1981). However, as these surface lakes have generally been observed to refreeze
90   on the ice-shelf surface at the end of each austral summer, with to date, no evidence of meltwater drainage into moulins, limited mass is lost through surface melting. Instead, mass has been mostly lost due to high basal melt rates (Adusumilli et al., 2020), attributed to the warm Circumpolar Deep Water (CDW) current that extends under the entire length of the GVIIS (Holland et al., 2010; Pritchard et al., 2012), though rates of basal melting are greatest at the southern end of the GVIIS (Adusumilli et al., 2020; Smith et al. 2020). These high basal melt rates have resulted in sustained thinning rates (Pritchard et al. 2012), which
95   together with frontal calving (Pearson and Rose, 1983; Reynolds and Hambrey, 1988), have contributed to the ice shelf's negative net mass balance since at least 2003 (Rignot et al. 2013; Paolo et al., 2015). Rignot et al. (2019) estimated that the GVIIS lost 9 Gt in 2017, compared to a balance flux of 70 ± 4 Gt yr^{-1}. GVIIS is thus a significant contributor to cumulative mass loss from the AP as a whole, which averaged -24 Gt yr^{-1} from 1979 to 2017.

On the northern GVIIS, there are three types of surface lake patterns. The principal pattern of lakes, which are generally the
100   largest in area, is aligned with the ice flowlines (Reynolds, 1981; Smith et al., 2007). This set of lakes is intersected by a second pattern of generally smaller, ribbon-type lakes, which lie parallel to the prevailing wind (Reynolds, 1981), suggesting that wind processes initiate the surface depressions that meltwater then fills. These first two sets of lakes appear to remain in similar locations each year due to the ice shelf's compressive flow, i.e. unlike the situation on most ice shelves where lakes move with ice flow towards the shelf front (Banwell et al., 2014). The third set of lakes are the deepest and exist within pressure ridge
105   complexes along the western margin of the ice shelf, onto which ice-shelf flow is directed (Reynolds, 1981). These lakes are therefore en-echelon in shape and propagate along the ice-shelf margin, hence have been referred to as 'travelling lakes' (LaBarbera and MacAyeal, 2011).

Unlike other AP ice shelves that have fully or partially disintegrated due to high rates of surface and/or basal melting, the retreat of GVIIS thus far has been relatively gradual, despite this ice shelf having the most extensive meltwater ponding and
110   the longest history of surface lakes of any AP ice shelf (Smith et al., 2007). This is likely due to the GVIIS' unique geographical setting with its dominantly compressive flow regime, as described above.

In this study we focus on the northern area of the GVIIS only; defined as our Area Of Interest (AOI) (see Fig. 1b, location shown by the red outline) with a total area of 7850 km^2. This is the region where a high density of surface lakes are often observed each melt season.

115   **3. Data and Methods**

Briefly, to quantify our understanding of surface melt over north GVIIS for the austral summers from 1979/1980 to 2019/2020, we analyse large-scale melt information from 25-km gridded passive microwave observations for both the AP and the northern GVIIS. For north GVIIS, these data are corroborated by smaller scale (4.45-km) active microwave observations available from

2007 to 2020. For austral summers from 2013/2014 to 2019/2020, we also calculate areas and volumes of ponded meltwater

120   on the northern GVIIS from all available cloud-free optical images from the Landsat 8 (from 2013) and Sentinel-2 (from 2017) satellites. Both our passive microwave-derived melt and optical image-derived surface ponding results are evaluated alongside surface air temperature and wind data from the BAS Fossil Bluff AWS (from 1979) on the northwest margin of the GVIIS (Fig. 1b, yellow star).

3.1 Large-scale microwave radiometer observations of melt

125   Large-scale melt information over the AP, including the GVIIS, was derived from microwave radiometer observations using the 1979 to 2020 near-daily 25-km melt product (version 2) of Picard et al. (2007) and Picard and Fily (2006), distributed on a polar stereographic grid. This melt/no-melt product, which has been used in several previous studies (e.g., Brucker et al., 2010; Magand et al., 2008; Wille et al., 2019), is based on the algorithm of Torinesi et al. (2003) that identifies the higher microwave brightness temperatures corresponding to melt using the radiation observed at 19 GHz in horizontal polarization.

130   If the observed brightness temperature on a given day exceeds an empirical threshold (defined by the mean and variability of the brightness temperatures observed during the previous winter season, when melt did not occur), the algorithm reports melt in the 25 km grid cell. Throughout this paper, we use the word ''melt' when referring to the presence of liquid meltwater (either in the near-surface snow, or on the surface) per the microwave data, but note that we are not referring to the process of active melting; information that specific cannot be obtained from passive microwave data.

135   The 1979 to 2020 brightness temperature time series was acquired by five successive sensors. The Scanning Multichannel Microwave Radiometer (SMMR), on the Nimbus 7 satellite launched in late October 1978, collected data at 18 GHz (while the sensor operated every other day, daily-averaged brightness temperatures were used as input). Starting in 1987, the series of Special Sensor Microwave Imager (SSMI) sensors on the Department of Defense Meteorological Satellite Program (DMSP) platforms F8, F11, F13 and F17 collected data at 19 GHz. Of note, there was a significant data gap between December 3, 1987

140   and January 14, 1988, and therefore we do not include any data from this melt season in our analysis. Although the melt data are provided with a spatial resolution of 25 km, the radiometers' 3-dB field of views at 19 GHz are larger (e.g., 69 km x 43 km for SSMI). Grid cells with elevations > 1700 m a.s.l. were masked out in Figs. 2 and S1.

Microwaves are sensitive to the presence of meltwater from the surface to the firn layers. Based on radiative transfer simulations, radiometer brightness temperatures at 19 GHz are typically sensitive to melt down to a snow depth of ~2 m (Picard

145   et al., 2007; Leduc-Leballeur et al., 2020). Wet snow has a very high emissivity compared to dry snow, but a flat surface of liquid water has a low emissivity as well. Therefore, at the transition from dry to wet snow, brightness temperatures increase quickly (i.e. indicating the presence of meltwater), but if melt intensifies, resulting in the formation of surface lakes, the brightness temperatures decrease. Cautious interpretation of the "melt days" maps is therefore required, particularly if surface ponding represents a large proportion of the grid cells.

150   For austral melt seasons from 1979/1980 to 2019/2020 (apart from 1987/1988 due to its missing data), and for each 25-km grid cell, we calculated the daily time series of microwave radiometer-derived melt/no melt, and the cumulative melt days each melt season (defined as November 1 to March 31 inclusive). This was done for both the whole AP (i.e. extent of Fig. 1a) and for the northern GVIIS AOI (Fig. 1b, red outline).

3.2 Small-scale microwave scatterometer observations of melt

155   For the northern GVIIS, we also derive small-scale melt information from an enhanced resolution C-band (5.225 GHz) VV polarization radar backscatter image time series collected by EUMETSAT's Advanced SCATterometer (ASCAT), aboard the tandem polar-orbiting satellites MetOp-A and MetOp–B. The 4.45 km enhanced product is obtained by applying the Scatterometer Image Reconstruction (SIR) algorithm with filtering (Lindsley and Long, 2016). The effective spatial resolution was estimated at ~12-15 km; three-fold finer than the effective resolution of the SMMR/SSMI based product (~50 km). For

160   each day, and for each grid cell, melt is assumed to be present when the ASCAT signal is lower than the winter mean signal minus 3 dB (Ashcraft and Long, 2006). Where snow and firn layers are completely frozen, the C-band penetration depth is of the order of meters to tens of meters, but where snow and firn layers have a high volumetric fractions of meltwater, the penetration depth is likely to be up to 10s of centimetres only (Weber Hoen and Zebker, 2000). As the penetration depth at 5 GHz in dry snow/firn is larger than at 19 GHz, ASCAT C-band radar is likely to be more sensitive to melt at depth than

165   microwave radiometers at 19 GHz.

For austral summers from 2007 to 2020, we calculate cumulative melt days per season over our study AOI. As this paper primarily focuses on surface and near-surface melt, rather than subsurface melt, and as ASCAT data are only available for 13 years, we primarily use the microwave radiometer data in this paper (Section 3.1).

3.3 Landsat 8 and Sentinel-2 derived meltwater areas and volumes

170   To calculate the time series of areal extents, depths, and therefore total volumes of surface meltwater lakes on the northern GVIIS for the seven austral summers from 2013/2014 to 2019/2020, we applied the threshold-based algorithm developed by Moussavi et al. (2020) to selected (see paragraph below) to multispectral imagery from Landsat 8 (30 m resolution, from 2013) and Sentinel-2 (10 m resolution, from 2017). Technical specifications for Landsat 8's Operational Land Imager (OLI) data are available online from NASA (https://landsat.gsfc.nasa.gov/operational-land-imager-oli/) and for Sentinel-2's MultiSpectral

175   Instrument (MSI), data are available online from ESA (https://sentinels.copernicus.eu/web/sentinel/technical-guides/sentinel-2-msi). The method, developed separately for each sensor, combines separate threshold-based algorithms to detect (1) lakes, (2) rocks, and (3) clouds. The various threshold values were determined by creating a training dataset based on selected Landsat 8 and Sentinel-2 images. Most notably, to classify liquid water-covered pixels, the Normalized Difference Water Index (NDWI) is used (Pope et al., 2016; Bell et al., 2017) with a threshold of NDWI > 0.19 for both sensors. Subsequently, to

180   calculate the water depths of those pixels determined to be water-covered, Moussavi et al. (2020) apply a physically-based algorithm that has more commonly been applied in Greenland (Sneed and Hamilton, 2007; Banwell et al., 2014; Pope et al.,

The Cryosphere
Discussions
Open Access
EGU

2016), and more recently, Antarctica (Dell et al., 2020). This algorithm calculates lake water depth using the rate that sunlight passing through a water column is attenuated with depth, lake-bottom albedo, and optically deep water reflectance (Philpot, 1989).

185   All Landsat 8 and Sentinel-2 images acquired from November 1 to March 31 each austral summer with a solar angle of > 15 degrees, with ≥ 0.45 km^2 water-covered pixels (equivalent to 500 Landsat pixels, or 4500 Sentinel-2 pixels), and which overlapped our study's AOI (Fig. 1b, red outline), were analysed using the methods described above. Once the images had been analysed, all tiles with the same date were mosaiced together and then clipped to a mask of our AOI in the Geographic Information System package, QGIS v3.2. In total, for Landsat 8, we analysed mosaiced images for 191 dates from December

190   6, 2013, to March 12, 2020, and for Sentinel-2, we analysed mosaiced images from 14 dates from January 3, 2017, to January 19, 2020. Of those images, nine Landsat 8 and Sentinel-2 image mosaics had the same dates, so we merged those; first, by resampling the Sentinel-2 data (10 m resolution) to the resolution of Landsat (30 m), and second, by taking overlapping water-covered cells in preference to dry pixels, and by taking the largest depths of the overlapping water-covered pixels. This resulted in a time series of 196 mosaiced images from December 6, 2013, to March 12, 2020. Errors and uncertainties associated with

195   lake area and depth retrieval methods for each sensor are thoroughly discussed in Moussavi et al. (2016, 2020) and Pope et al. (2016).

   Due to temporally varying satellite paths and/or cloud cover, only 11 out of the 196 mosaiced images covered the entirety of our AOI (Table S1). Therefore, to be able to compare areas and volumes of surface meltwater on dates with incomplete AOI coverage, we first created a mask of all pixels that were wet on at least one of the 196 dates analysed from 2013 to 2020

200   (Williamson et al. 2018), hereafter called a '*maximum wetted area mask*'. Second, we created a '*maximum volume mask*' by assigning all wet pixels in the *maximum wetted area mask* a depth equal to the maximum water depth observed out of all 196 images. Finally, for each image mosaic with ≥ 10% cloud-free coverage of our AOI (113 image dates), we normalized their total area and total volume of meltwater to our entire AOI using the following approaches. For each mosaiced image, we calculated the total observed meltwater area as a fraction of the total wetted area mask for the equivalent area. This fraction

205   was then multiplied by the total area of the *maximum wetted area mask* over the whole AOI. To normalize the meltwater volume to the AOI, we did likewise, but instead used the *maximum volume mask*.

3.4 Local weather station data

   We analyse the only available local AWS data in order to investigate the possible atmospheric driver(s) of the exceptional melt event over north GVIIS in 2019/2020. Near surface (2 m) temperature, relative humidity, wind direction, and wind speed data

210   are available from the BAS Fossil Bluff AWS (Fig. 1b, yellow star, location: -71.329 S, -68.267 W), at 12-hour intervals from 1979 to 1999, and at 5 or 10 minute intervals from 1999 to 2020. However, significant data gaps are present between 1999 and early 2007.

First, we compare the 2019/2020 daily mean temperatures with the daily mean temperatures from 1979 to 2020 (using 12-hour data); i.e. the complete time period that we also have microwave radiometer data for. Second, for 2007 to 2020, which is when

215 AWS data are at a high frequency (10 minutes) and data gaps are minimal (six months in the total record were missing values, but these were < 15% of the expected total for each of those months), we calculate the length of time periods (in hours) when surface air temperatures are continuously ≥ 0°C during each melt season. We also consider the occurrence of foehn winds, which are hot, dry winds often produced on the leeward side of mountains (Cape et al., 2015; Elvidge et al., 2016). Over GVIIS, the steep topography that generates foehn flow is provided by Alexander Island. We analyse foehn wind occurrence

220 using a modified version of a metric previously used over the Larsen C Ice Shelf (Datta et al., 2019; Weisenneker et al., 2018), whereby a 'foehn condition' is considered to initiate when air temperatures increase by ≥ 1°C, wind speed increases by ≥ 1.5 ms^{-1} and relative humidity decreases by ≥ 5%. We use a wind speed threshold of 1.5 ms^{-1}, instead of the higher threshold of 3.5 ms^{-1} used by Datta et al. (2019) for the Cabinet Inlet AWS, to account for lower mean wind speeds over north GVIIS. This foehn condition is assumed to remain until the conditions (with respect to the period preceding the foehn condition) are no

225 longer met. Finally, we also examine differences in atmospheric regimes (temperature, wind direction and speed) within each wind direction class (northeasterly, northwesterly, southeasterly and southwesterly).

We note that it is beyond the scope of this study for us to identify specific meso-scale drivers of this exceptional melt event, especially as 2019/2020 is not a record melt season for the AP as a whole (see Section 4.1), and regional climate models frequently struggle to resolve localized surface melt in regions with highly-variant topography (Van Wessem et al., 2015),

230 such as the GVIIS and its surrounding region.

4. Results

4.1 Microwave radiometer-derived melt observations over the Antarctic Peninsula

For the AP, the spatially-averaged cumulative melt days in the 2019/2020 austral melt season is 47 days (Fig. 2b), which is 53% higher (Fig. 2c) than the spatially-averaged climatology from 1979/1980 to 2019/2020 (31 days; Fig. 2a). However, of

235 these 41 melt seasons, the 1992/1993 melt season has the highest spatially averaged cumulative melt days over the AP (62 days; Fig. S1). During that 1992/1993 season, although cumulative melt days over north GVIIS were only slightly higher than the 1979/1980 to 2019/2020 mean (Fig. S1d), cumulative melt days on the Larsen C Ice Shelf were particularly high, with a maximum of 117 cumulative melt days in the southern area of the ice shelf (Fig. S1c). Nonetheless, using active microwave data from ASCAT, Bevan et al. (2020) reported that Larsen C experienced a record high melt year in 2019/2020.

240
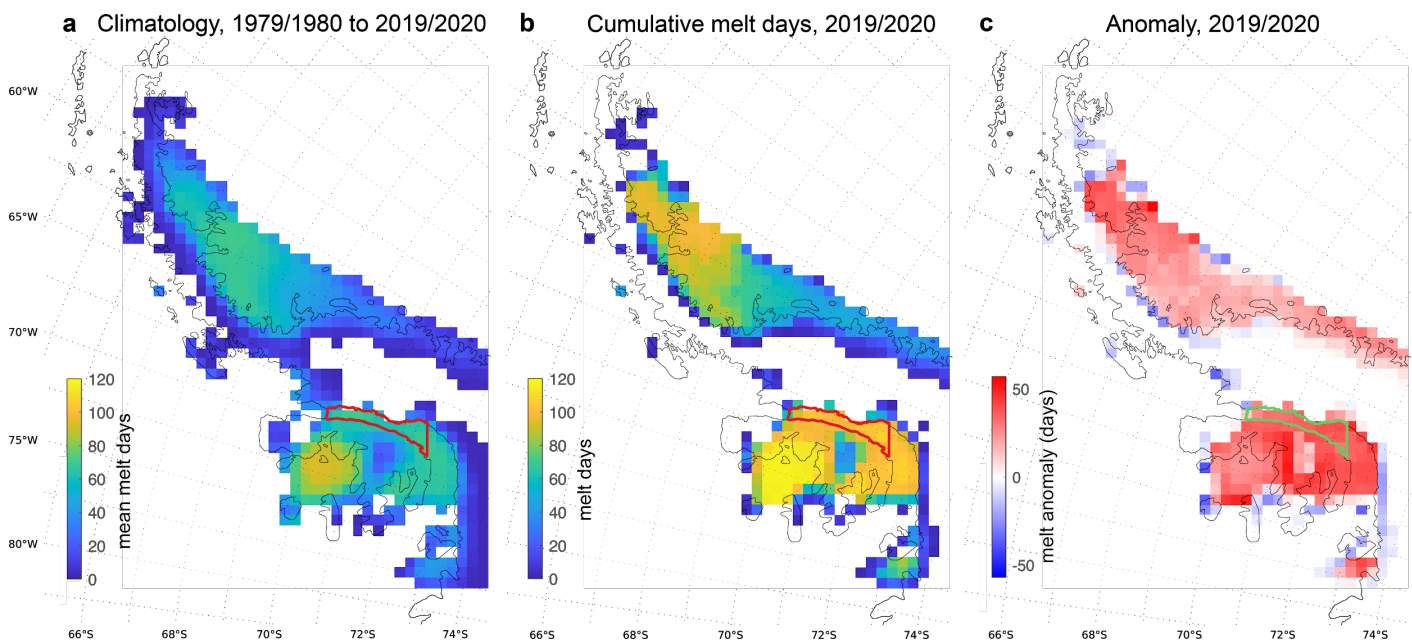
Figure 2. Microwave radiometer-derived maps of surface/near-surface melt days over the AP. (**a**) the climatology (i.e. mean cumulative melt days per season) from 1979/1980 to 2019/2020 (excluding 1987/1988 due to missing data); (**b**) cumulative melt days in 2019/2020; (**c**) the 2019/2020 melt season anomaly (i.e. (b) minus (a)). Melt days are counted within the period November 1 to March 31 (inclusive) each austral summer. The location of the study AOI is shown by a red outline in panels a) and b), and as a green outline in panel c). The black outline of the AP is from the MODIS Mosaic of Antarctica (Haran et al., 2014).

4.2 Microwave-derived melt observations over north GVIIS

Over the northern GVIIS, microwave radiometer-derived spatially-averaged cumulative melt days over the study AOI (12 grid cells, total area = 7556 km^2) in the 2019/2020 austral melt season is 101 days (Figs. 3b and d), which is higher than for any other melt season since 1979/1980, and is 53% higher (Fig. 3c) than the spatially averaged climatology (66 melt days) from 1979/1980 to 2019/2020 (Figs. 3 and S2). However, as melt data for the 1987/1988 season are missing, we only conclude that 2019/2020 was the most significant melt season over 32 years. This result is supported by the analysis of scatterometer-derived melt data from ASCAT, which show that spatially-averaged cumulative melt days over the study AOI in the 2019/2020 austral melt season is 117 days; 70% higher than the spatially averaged climatology (69 melt days) from 2007/2008 to 2019/2020 (Fig. S3). The microwave radiometer-derived data suggests that 1989/1990 has the second highest spatially-averaged cumulative melt days (93) over the study AOI (Figs. 3d and S2).

Using the microwave radiometer data to consider the cumulative days of melting occurring over 100% of the AOI each season, 2019/2020 also sees the highest such number of days, 93 (Fig. 3d, dark blue bars), and 1989/1990 sees the second highest

9

number of days (85). These values can be compared to a mean value of 53 cumulative melt days over 100% of the AOI from 1979/1980 to 2019/2020. Note that for each season, we do not specifically consider the mean areal extent of melting as this variable is found to be almost directly proportional ($r^2 = 0.9973$) to the spatially-averaged cumulative melt days (Fig. S4).

In terms of intra-annual patterns in percentage melt area over north GVIIS in 2019/2020, the microwave radiometer data shows

265 that 100% of the AOI area experiences melting every day from November 24, 2019, to February 22, 2020 (Fig. 4c). After February 22, the area of melting drops to 0% of the AOI over just three days, which is consistent with a drop in the mean daily air temperature (Fig. 4a). For a few weeks after February 25, the area of melting fluctuates significantly, consistent with the air temperature fluctuating around 0°C. On March 6 and 7, 2020, 100% of the AOI is observed to melt again. From March 16, 2020, no additional melting is observed. Compared to the mean melt area over the two time periods shown in Fig. 4c (i.e.

270 1979/1980 to 2019/2020, and 2013/2014 to 2019/2020), the observed melt area in 2019/2020 is 100% of the AOI for a significantly longer continuous period of 91 days.
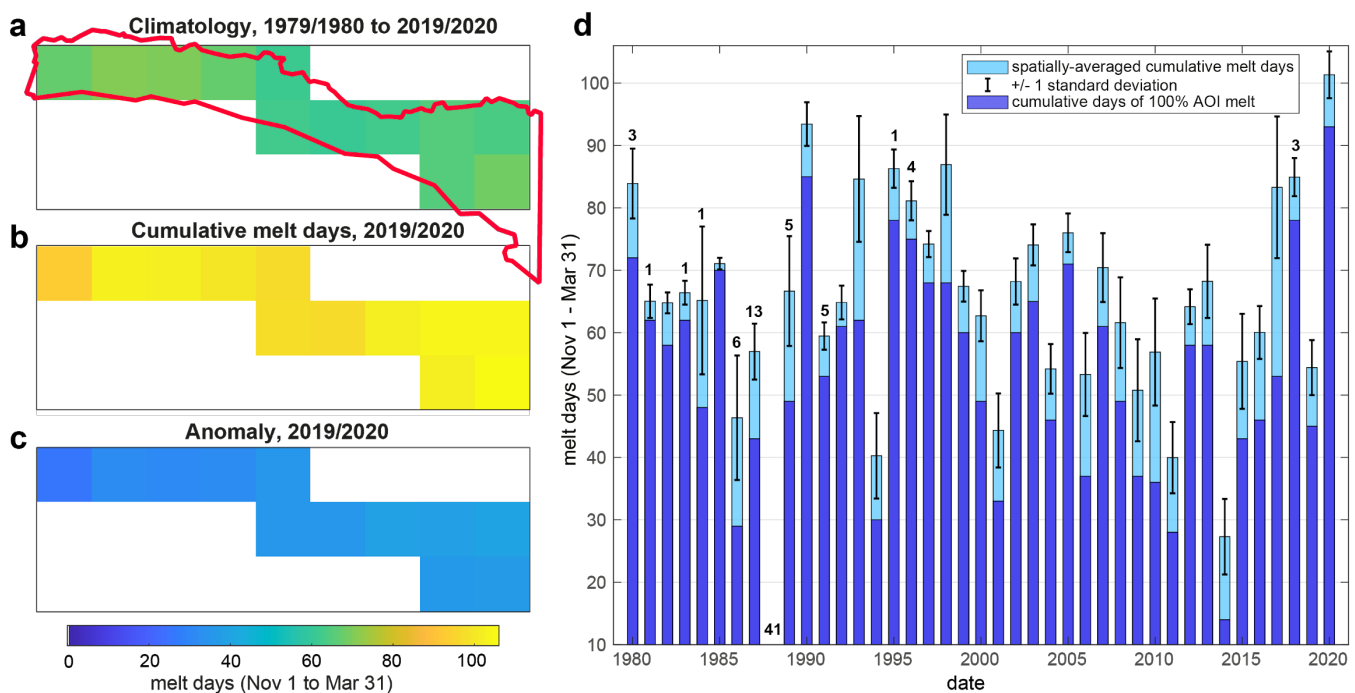
Figure 3. Microwave radiometer-derived cumulative melt days over the northern GVIIS AOI (see Fig. 1b for location, red outline). (**a** – **c**) Maps of surface/near-surface melt days per 25 km grid cell over north GVIIS from November 1 to March 31.

275 The relative location and shape of the study's AOI is shown by the red outline (also see Fig. 1b, red outline). White cells are those out of the AOI. (**a**) Mean cumulative melt days for each 25 km grid cell for austral summers from 1979/1980 to 2019/2020, apart from 1987/1988 due to data unavailability. (**b**) Cumulative melt days per grid cell in the 2019/2020 austral summer. (**c**) Anomaly of the 2019/2020 melt season (i.e. (b) minus (a)). (**d**) Light blue bars represent spatially-averaged (i.e. over the 12 grid cells in the AOI) cumulative melt days, for each austral summer from 1979/1980 to 2019/2020 (apart from

280   1987/1988). The x-axis dates indicate the second year of each austral summer, e.g., 2020 corresponds to the 2019/2020 season. Black error bars show +/- one standard deviation from the spatially-averaged cumulative melt days. Dark blue bars show cumulative days when the melt extent is 100% of the AOI for each summer from 1979/1980 to 2019/2020. For melt seasons with missing data, the total number of missing data days is indicated by the black number above the corresponding bar.

4.3 Optical image-derived meltwater areas and volumes over north GVIIS

From 2013 to 2020, when we have Landsat 8 and/or Sentinel-2 optical imagery available, the day with the maximum observed area ($1.2 \times 10^9 \, \text{m}^2$) and volume ($6.2 \times 10^8 \, \text{m}^3$) of ponded surface meltwater on the northern GVIIS was 19 January, 2020 (Figs. 1b, 4b, S5 and S6, Table S1), when 23% of the AOI's area is covered in ponded water. On this date, it is fortuitous that the whole of our AOI is visible in a mosaic of cloud-free Sentinel-2 image scenes (Fig. 1b; background image), and is also mostly

290   visible in a mosaic of Landsat 8 images acquired on 17 and 19 January (not shown). Calculated areas and depths of meltwater lakes on January 19, 2020, over the entire study AOI, are shown in Fig. S4, and the total meltwater volume on this date is shown in Fig. 4b. Unlike on other dates with much cloudier imagery, normalization of meltwater areas and volumes to the AOI on January 19 is not required (see Section 3.3 for more details, Fig. S6 for plots of both the observed and normalized meltwater areas and volumes for the 2013/2014 to 2019/2020 melt seasons, and Table S1 for all data).

295   In all the seven melt seasons analysed, ponded surface meltwater volumes do not peak until January or February (Fig. 4b). However, in 2019/2020, meltwater volumes start to increase rapidly in late December/early January, which is earlier than in any other season, and corresponds with above average air temperatures in late December 2020 (Fig 4a, also see Section 4.4 for analysis of local weather conditions). There is a notable decrease in surface meltwater ponding volume in mid to late January 2020, which corresponds with a substantial decrease in air temperatures in mid-January (Fig. 4a).

300   The second largest melt season in terms of meltwater ponding is 2017/2018, with a peak in total meltwater area ($4.6 \times 10^8 \, \text{m}^2$) and volume ($2.5 \times 10^8 \, \text{m}^3$) on 29 January, 2018 (Figs. 4b and S6). However, these values are less than half of the respective values measured on 19 January, 2020. Aside from 2019/2020 and 2017/2018 (i.e. the melt seasons with the greatest and second greatest volumes of surface ponding respectively), the other five melt seasons out of the seven analysed have relatively low volumes of ponded meltwater.
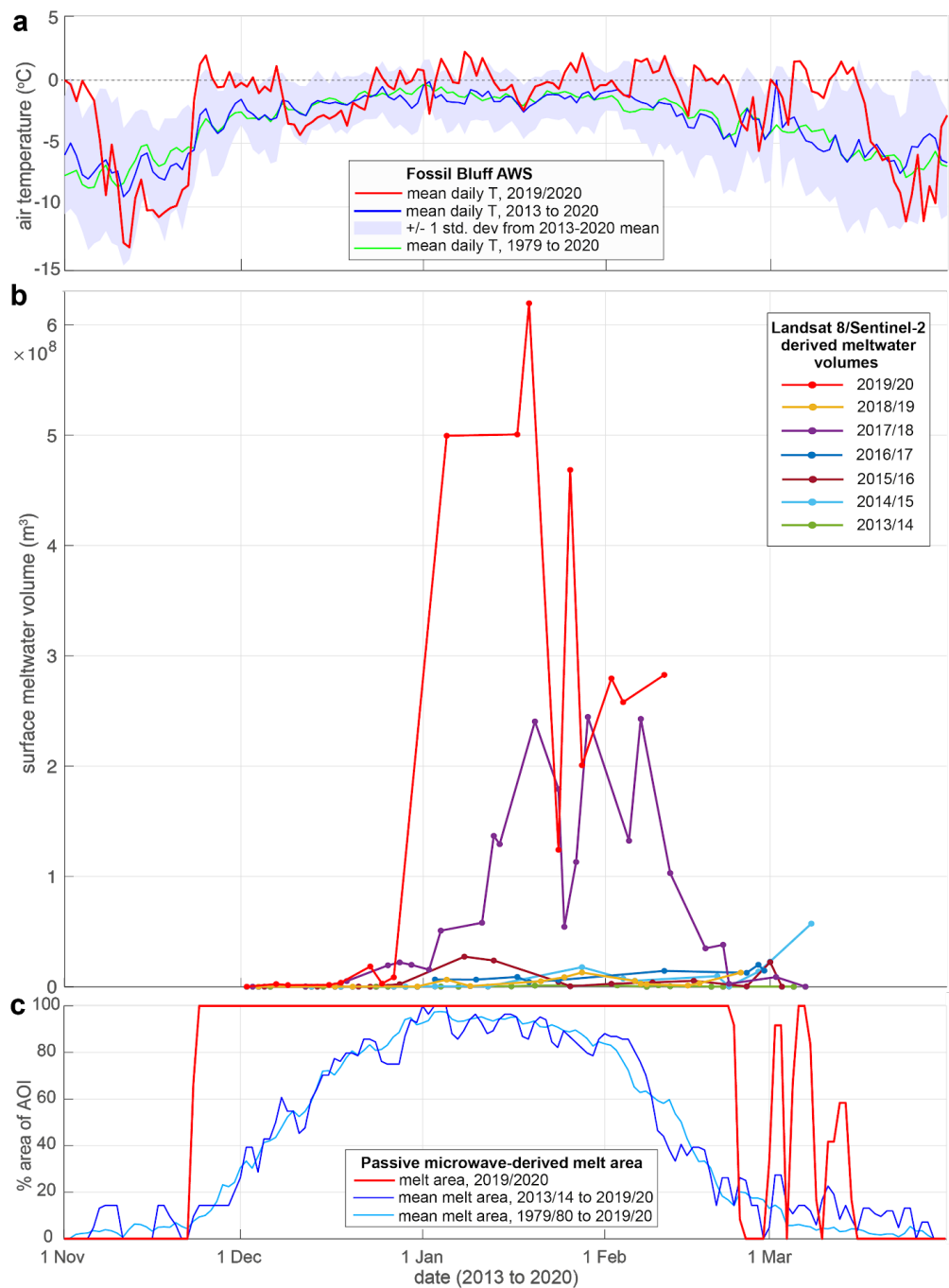
Figure 4 (a) Surface (2 m) air temperature data from the Fossil Bluff AWS (location in Fig. 1b, yellow star). The daily mean air temperature for the 2019/2020 melt season are shown by the red line, the daily mean for the 7 melt seasons from 2013/2014 to 2019/2020 are shown by the blue line, +/- one standard deviation from that blue line is shown by the areas of blue shading, and the daily mean temperature from 1979 to 2020 (using 12-hour data) is shown by the green line. The horizontal black

310   dashed line depicts 0ºC. (**b**) Calculated volumes of surface meltwater ponding in the GVIIS AOI from 2013/14 to 2019/20,
       derived from Landsat 8 and Sentinel-2 optical imagery, following Moussavi et al. (2020). Data from mosaiced images are only
       plotted if the image includes >10% of the study's AOI that is cloud free; data from mosaiced images on 113 images total are
       shown. On dates when imagery does not cover 100% of the AOI (Fig. 1, red outline), observed meltwater volumes are
       normalized to the AOI (see Section 3.3 for further details, and Fig. S5 for a plot of all the observed meltwater volumes). (**c**)

315   Microwave radiometer-derived near-surface melt extent over the GVIIS AOI (Fig. 1b, red outline) as a % of the total area
       (7556 km^2). Daily areas of melting for 2019/2020 are shown by the red line, the daily mean area of melting from 2013/2014
       to 2019/2020 is shown by the dark blue line, and the daily mean area of melting from 1979/1980 to 2019/2020 (excluding
   1987/1988) is shown by the light blue line.

4.4. Near-surface atmospheric conditions

Analysis of the mean daily surface air temperatures (derived from 12-hour values) from the Fossil Bluff AWS from 1979 to
2020 indicates that 2019/2020 is anomalously warm over five multi-day periods starting in late November (Figs 4a and S7).
During these periods, mean daily air temperatures are ≥ 0ºC for sustained time periods of up to a week. The total positive
degree days for the 2019/2020 melt season (Nov 1 to March 31 inclusive) is 40, compared to a mean of 19 ± 14 days (mean ±

325   1 standard deviation) from 1979/1980 to 2019/2020.

We further analyse the high-resolution (10 minute) AWS data from 2007 to 2020 to identify periods of sustained high
temperatures, as these will be periods where it is possible that no refreeze at all occurred during the diurnal cycle, potentially
enhancing the surface melt-albedo effect. We find that the longest continuous period when air temperatures are ≥ 0ºC in
2019/2020 is 90 hours in early February (Fig. 5, cyan line, and Fig. 6, label C). The longest five such time periods in 2019/2020

330   are labelled A to E in Fig. 6, and it is notable that two pairs of periods, A and B, and C and D, are only separated by a matter
       of hours. The mean length of these five longest periods of temperatures ≥ 0ºC in 2019/2020 is 61 hours, which is higher than
       for any other season in the record (Fig. 5, black line). Considering all recorded temperature data in each melt season (November
       1 to March 31), a higher percentage (33%) of 2019/2020 has air temperatures ≥ 0ºC compared to any prior season (Fig 5, red
       line).

335   We also examine the potential role of foehn winds on driving melt in 2019/2020. Foehn conditions (as described in Section
       3.4) are only present for about 9 hours over the entire 2019/2020 season (Fig 5, blue line), and occur in early and late summer
       (Fig. 6b, blue circles) when winds are typically stronger. The total time during each season when foehn conditions are
       calculated from AWS data has been relatively low since the 2007/2008 and 2008/2009 melt seasons, which each had a total of
       about 72 hours of foehn flow (Fig. 5).

340
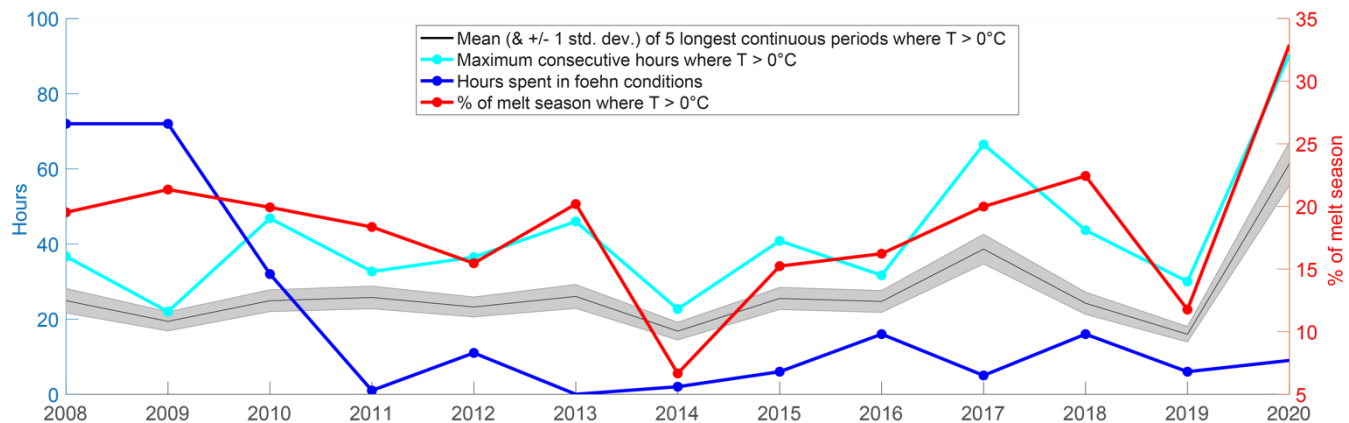
Figure 5. Analysis of sustained warm (≥ 0ºC) air temperature (T) periods and foehn wind occurrence for the 2007/2008 to 2019/2020 melt seasons. The cyan line shows the maximum number of consecutive hours in each melt season when T ≥ 0ºC. The black line shows the mean length (hours) of the five longest periods when T ≥ 0ºC for each season, with the grey shading

345 indicating +/- 1 standard deviation from that mean. The red line shows the proportion of each season (November 1 to March 31) when T is ≥ 0ºC. The blue line shows the total number of hours spent in a foehn condition (see Section 3.4 for definition) each season. The x-axis dates indicate the second year of each austral summer, e.g., 2020 corresponds to the 2019/2020 season.

Considering wind direction alongside air temperature for melt seasons from 2007 to 2020, the climatology indicates that

350 northwesterly winds dominate flow at all temperatures (Fig. 7a), but are more dominant when temperatures are ≥ 0ºC (Fig. 7b), and are even more so when we limit analysis to just the five longest periods of sustained temperatures ≥ 0ºC in each season. However, in the 2019/2020 season, northwesterly winds are less dominant, especially when only temperatures ≥ 0°C are considered (39% vs 47%; Fig. 7b), and further limited when only the five longest periods of sustained temperatures ≥ 0°C (Fig. 6; periods A-E, Fig 7c) are considered (37% vs. 59%; Fig. 7c). Instead, the proportions of wind coming from the northeast

355 are higher in 2019/2020 compared to the climatology (26% vs 24%), particularly when temperatures are ≥ 0ºC (32% vs 24%).

The 2007 to 2020 climatology shows that, as expected, northwesterly winds typically include a higher proportion of warm, fast winds, than other wind directions (Fig. S8a), whereas, northeasterly winds are typically lower-speed overall, and are generally colder (Fig. S8b). However, in the 2019/2020 melt season, we show that both northwesterly and northeasterly winds show warmer temperatures at lower wind speeds.
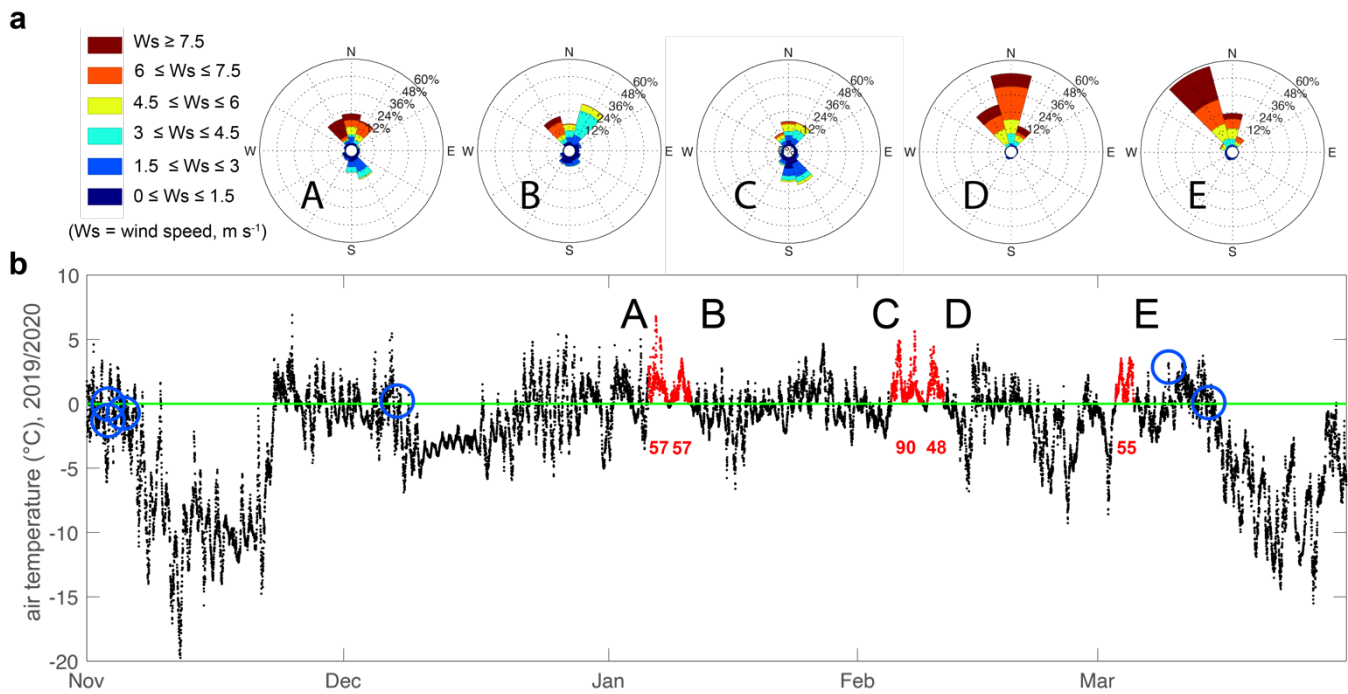
360

Figure 6. 2019/2020 air temperature and wind data (10 minute) from the Fossil Bluff AWS. (**a**) Wind roses for corresponding periods of sustained air temperatures (A-E) indicated in b. (**b**) Air temperature record for 2019/2020 with the five longest periods of temperatures ≥ 0ºC shown in red. The red numbers below these time periods indicate the total number of hours when the temperature is continuously ≥ 0ºC. It is notable that only 9 hours separate periods A and B, and only 14 hours separate C and D. The six blue circles indicate periods when we calculate foehn conditions to be present (see Section 3.4 for methods).
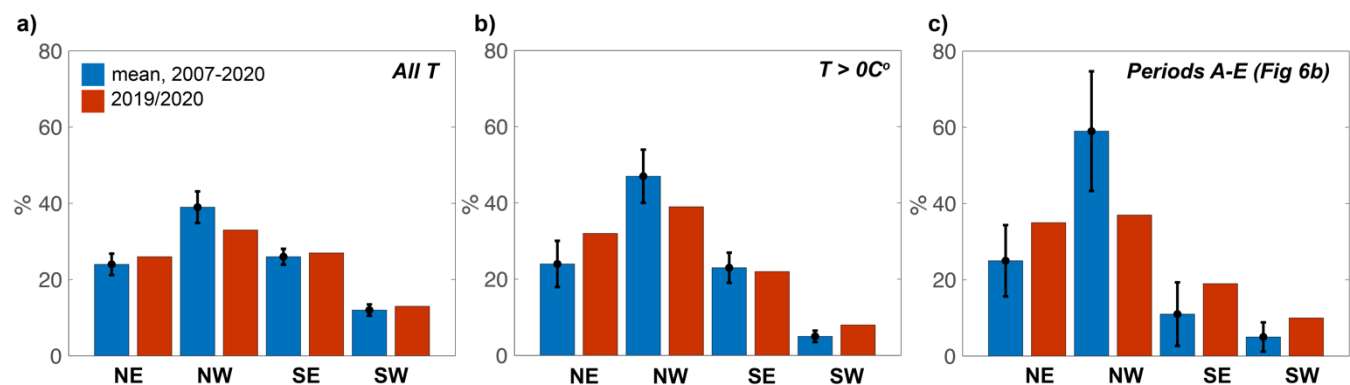
Figure 7. Percentage (%) of wind each season (November 1 to March 31) at Fossil Bluff AWS that is northeasterly (NE), northwesterly (NW), southeasterly (SE), southwesterly (SW), with the interannual (2007/2008 to 2019/2020) mean shown in blue and the 2019/2020 values shown in red. (**a**) Wind direction proportions using all recorded air temperatures. (**b**) Wind

15

direction proportions only when recorded temperatures are ≥ 0ºC. (**c**) Wind direction proportions only during the five longest periods of T ≥ 0ºC (A to E, Fig 6b) for all melt seasons (blue) and for 2019/2020 (red).

375

5. Discussion

5.1 Comparison of the optical image and microwave-derived melt data over north GVIIS, 2013 to 2020

Microwave melt data are binary (i.e. there is either melt or no melt), thus these data do not measure the intensity of the melting, nor the volume of meltwater present. Additionally, while the optical data are used to detect the presence of surface meltwater,
380 the microwave radiometer data can contain melt information down to a snow depth of < 2 m, depending on the presence of surface lakes, and/or wetness of the subsurface snow/firn (see Section 3.1 for more detail). Therefore, we cannot easily directly compare the microwave-derived melt data with the optical image-derived ponding data. However, together, these data are informative on the time it takes between melt onset and surface ponding over the northern GVIIS, and likewise at the end of the season.

385 For the time period from 2013/2014 to 2019/2020, when we have three independent datasets, 2019/2020 was anomalous for the following reasons. Optical imagery indicates this season had the largest volumes of observed surface meltwater ponding (Fig. 4b), microwave radiometer and scatterometry data show that it also had the most spatially extensive melt (i.e. 100% of the AOI) for the greatest number days (Fig. 3d), and the highest number of cumulative melt days (Figs 3d, S2 and S3).

In the 2019/2020 season, the microwave radiometer data first indicate the presence of surface/near-surface melt on November
390 22, which is present over 100% of the AOI by November 24 (Fig. 3c). However, it isn't until mid-December that surface meltwater ponding is observed in the optical imagery (Fig. 4b). This offset in the timing of the observations is likely because although sustained positive air temperatures in late November 2020 increased surface and near-surface melt rates, it takes time for surface ponds to develop, and this will only happen if suitable surface and firn/ice conditions are present. Towards the end of the melt season, although there are no cloud-free Landsat 8 or Sentinel-2 images available after mid-February 2020 (Fig.
395 4b), our visual analysis of MODIS imagery suggests that open water lakes remain until at least February 25, with some lakes potentially remaining until mid to late March. Meanwhile, our microwave radiometer-derived melt drops to zero by February 25, but then fluctuates until mid-March (Fig. 4c); perhaps indicative of a melt/refreeze process.

5.2 Near-surface/surface melting over north GVIIS, 1979 to 2020

From 1979/1980 to 2019/2020 (excluding 1987/1988), the microwave radiometer data show that 2019/2020 was the largest
400 melt season over the northern GVIIS in terms of the most spatially extensive melt (i.e. 100% of the AOI) for the greatest number days (Figs 3 and S2), and greatest number of spatially-averaged melt days; results that are corroborated by our scatterometer-derived melt data from 2007 to 2020 (Fig. S3a-c). As mentioned in Section 3.2, scatterometer-derived

16

cumulative melt days (117 days) are likely higher than those derived from the radiometer data (101 days; Fig. S3d) because C-band radiation has a larger penetration depth, thus likely detects melt at greater depths (Weber Hoen and Zebker, 2000).

405   The microwave radiometer data suggest a slightly negative trend in cumulative melt days and areal melt extent (Figs. 2, 3d and S2) from the mid 1990s until ~2015/2016, which is consistent with negative near-surface air temperature trends over the AP until 2016, likely relating to oscillations in the Southern Annular Mode (SAM) (Picard et al., 2007; Turner et al., 2016). This temperature trend is in contrast to the years prior to the mid/late 1990s, when trends over the AP were generally positive since the 1950s (though this is not apparent in our microwave radiometer-derived melt data).

410   Although this study does not analyse optical imagery over the northern GVIIS prior to the 2013/2014 season, we suggest that 2019/2020 may have also had the largest volumes of surface meltwater ponding out of the prior 31 seasons for the following two reasons. First, for the period 2013/2014 to 2019/2020 when we have three independent data sets, all data show that 2019/2020 had the most melt (see Section 5.1). Second, for the period 1990/1991 to 2012/2013, the microwave data show that, compared to the 2019/2020 season, no melt season had either a greater number of days of: i) spatially-averaged cumulative
415   melt, or ii) 100% AOI melt.

5.3 Local climatic controls of the 2019/2020 melt event

Our air temperature analysis using both daily averages (from 1979; Fig. S7), and higher temporal resolution (10 minute) data (from 2007; Fig. 6b), shows anomalously long time periods when air temperatures were continuously ≥ 0°C in 2019/2020. Using the 10-minute data, the longest such period was 90 hours in 2019/2020, suggesting that zero re-freeze happened during
420   that time (Fig. 6b). Overall, 2019/2020 also had the highest proportion of time (33% of the season) when temperatures were above ≥ 0°C (Fig. 5). We suggest that the sustained periods of warm temperatures, which started unusually early in the melt season, both initiated and enhanced melting in 2019/2020. The presence of just a small quantity of surface meltwater early in the melt season is especially important as this will have a disproportionately high effect on overall surface melt production due the non-linear melt-albedo feedback process (Trusel et al., 2015).

425   Compared to the 2007 to 2020 AWS record, the 2019/2020 austral summer experiences a lower proportion of northwesterly wind (Fig 7), though these winds are warmer at lower speeds (Fig. S8a). Instead, the proportion of northeasterly wind is higher in 2019/2020 compared to the 2007 to 2020 climatology (Fig. 7), and these winds are also warmer at lower speeds (Fig. S8b). We therefore suggest that warmer, lower speed, northwesterly and northeasterly wind helped to drive melting in 2019/2020. We note that a record high Indian Ocean Dipole (IOD) in the early part of the 2019/2020 melt season is discussed in Bevan et
430   al. (2020) as a potential large-scale driver for warm, northerly surface winds on the western AP.

Although warm foehn winds are known to initiate periods of sustained melt and/or produce firn densification due to near surface melt and refreezing (Luckman et al., 2015), our analysis suggests that the 2019/2020 melt season experienced limited foehn conditions (see Section 3.4) in the early, and then late, melt season (Fig. 6b). This is predictable foehn flow behaviour, e.g., over the Larsen C, foehn winds are stronger in the shoulder seasons, and especially winter, when wind speeds are generally

435   higher (Datta et al., 2019; Wiesenneker et al., 2018). Our observation of minimal foehn wind conditions in 2019/2020 is consistent with our observation of an overall decrease in the frequency of northwesterly winds (Fig. 7), which are typically responsible for foehn flow.

As also noted earlier, in this study we chose to focus on identifying local climate drivers of this exceptional melt event rather than trying to establish large-scale atmospheric drivers. This was because we do not find that 2019/2020 is a record melt season

440   for the AP as a whole (see Section 4.1) and regional climate models often struggle to resolve localized surface melt in regions with highly-variant topography (Van Wessem et al., 2015) such as north GVIIS.

6. Conclusions

We have used microwave radiometer data back to 1979, and microwave scatterometer data back to 2007, to show that the 2019/2020 austral melt season on the northern GVIIS was exceptional in terms of both cumulative melt days and areal extent

445   compared to the previous 31 melt seasons since 1988/1989, and possibly since 1979/1980. We also used optical satellite imagery back to 2013 to show that the observed surface meltwater ponding on the northern GVIIS in 2019/2020 was also exceptional since at least 2013/2014.

Our analysis based on the local weather data from the Fossil Bluff AWS shows that sustained periods of warm ($\geq 0°C$) temperatures from early in the season (late November) likely contributed to the exceptional 2019/2020 melt event. These

450   periods of sustained warm temperatures were likely driven by warm northwesterly and northeasterly low-speed winds. Consistent with our finding that the proportion of northwesterly wind decreased in 2019/2020, we only calculate a total of ~9 hours of foehn flow for this season, which occurred in early and late summer.

Using Landsat 8 and Sentinel-2 satellite imagery, we observed the maximum volume of meltwater ponding on the northern GVIIS on January 19, 2020, when ~23% of our AOI was covered in surface lakes with a mean depth of 0.5 m. In comparison,

455   only 10% of the 3200 km^2 area of the Larsen B Ice Shelf that disintegrated in 2002 was covered in surface ponds with a mean depth of 0.8 m (Banwell et al., 2014). However, unlike the Larsen B Ice Shelf that had relatively unconstrained, and therefore, extensional ice flow (e.g. Scambos et al., 2004; MacAyeal et al., 2003), GVIIS has dominantly compressive flow, enabling the shelf to remain relatively stable despite large volumes of surface water (Lai et al., 2020). Despite this, our results show that some of the areas of dense surface ponding near the eastern margin of north GVIIS coincide with areas classified as vulnerable

460   to hydrofracture by Lai et al. (2020, their Fig. 4), particularly if pre-existing surface crevasses are present. Though individual years of exceptional high surface melt do work to decrease ice-shelf stability, further research is required to better constrain the potential timing and style of a GVIIS collapse event due to the competing controlling factors of surface melt, basal melt, and stress regime.

The Cryosphere
Discussions

465   *Code and data Availability.*   The code used to calculate areas and volumes of surface meltwater is available at
https://github.com/mmoussavi/Lake_Detection_Satellite_Imagery/ and described in detail in Moussavi et al. (2020). The
passive microwave melt product is available at http://pp.ige-grenoble.fr/pageperso/picardgh/melting/, last accessed on
October, 1 2020. The ASCAT enhanced resolution product is available at
https://www.scp.byu.edu/data/Ascat/SIR/msfa/Ant.html, last accessed on October 1, 2020. Temperature data are available
470   from the BAS Fossil Bluff AWS at 10 minute intervals from 2006 to 2020 here: https://legacy.bas.ac.uk/cgi-bin/metdb-form-
2.pl?tabletouse=U_MET.FOSSIL_BLUFF_ARGOS&complex=1&idmask=.....&acct=u_met&pass=weather), and at
intervals ranging from 12 hour to 1 hour from 1979 to 2006 here: https://legacy.bas.ac.uk/cgi-bin/metdb-form-
2.pl?tabletouse=U_MET.FOSSIL_BLUFF_SYNOP&complex=1&idmask=.....&acct=u_met&pass=weather)

Author contributions.   AFB conceived the study, analysed the optical image-derived and microwave-derived melt data, and
475   drafted the manuscript. RTD performed the local climate analysis. MM derived surface meltwater areas and volumes from the
optical satellite imagery. RD further processed the optical imagery-derived results. LB and GP processed the microwave
radiometer and scatterometer data to produce the melt data. CAS identified key Landsat 8, Sentinel-2 and MODIS imagery for
initial analysis. All authors discussed the results and were involved in editing of the manuscript.

Competing interests.   The authors declare that they have no conflict of interest.

490

References

Adusumilli, S., Fricker, H.A., Medley, B. et al., Interannual variations in meltwater input to the Southern Ocean from
Antarctic ice shelves. Nat. Geosci. https://doi.org/10.1038/s41561-020-0616-z, 2020.

19

The Cryosphere
Discussions

Open Access

EGU

Arthur, J. F., Stokes, C., Jamieson, S. S., Carr, J. R., & Leeson, A. A. (2020). Recent understanding of Antarctic supraglacial
495   lakes using satellite remote sensing. Progress in Physical Geography: Earth and Environment.
https://doi.org/10.1177/0309133320916114

Ashcraft and Long, D., Comparison of methods for melt detection over Greenland using active and passive microwave
measurements, International Journal of Remote Sensing, 27, 12 - 14, 2469–2488.
https://doi.org/10.1080/01431160500534465, 2006.

500   Banwell, A. F., & MacAyeal, D. R., Ice-shelf fracture due to viscoelastic flexure stress induced by fill/drain cycles of
supraglacial lakes. Antarctic Science, 27, 587-597. doi: https://doi.org/10.1017/S0954102015000292, 2015.

Banwell, A. F., MacAyeal, D. R., & Sergienko, O. V., Breakup of the Larsen B Ice Shelf triggered by chain reaction
drainage of supraglacial lakes. Geophysical Research Letters, 40, 5872-5876. doi: https://doi.org/10.1002/ 2013GL057694,
2013.

505   Banwell, A.F., Cabellero, M., Arnold, N., Glasser, N., Cathles, L.M., MacAyeal, D., Supraglacial lakes on the Larsen B Ice
Shelf, Antarctica, and Paakitsoq Region, Greenland: a comparative study. Annals of Glaciology. 55(66),
doi:10.3189/2014AoG66A049, 2014.

Banwell, A. F., Willis, I. C., Macdonald, G. J., Goodsell, B. & MacAyeal, D. R., Direct measurements of ice-shelf flexure
caused by surface melt-water ponding and drainage. Nature Communications, 544, 349-352. doi:
510   https://doi.org/10.1038/nature22049, 2019.

Barrand, N. E. et al. Trends in Antarctic Peninsula surface melting conditions from observations and regional climate
modeling. J. Geophys. Res. 118, 315–330, 2013.

Bell, R. E. et al. Antarctic ice shelf potentially stabilized by export of meltwater in surface river. Nature 544, 344–348, 2017.

Bell, R. E., Banwell, A. F., Trusel, L. D., & Kingslake, J., Antarctic surface hydrology and impacts on ice-sheet mass
515   balance. Nature Climate Change, 8, 1044-1052. doi: https://doi.org/10.1038/s41558-018-0326-3, 2018.

Bevan, S., Luckman, A., Hendon, H., and Wang, G., Larsen C Ice Shelf surface melt is a 40-year record high, The
Cryosphere Discuss., https://doi.org/10.5194/tc-2020-130, 2020.

Brucker, L., Picard, G., & Fily, M., Snow grain-size profiles deduced from microwave snow emissivities in Antarctica.
Journal of Glaciology, 56(197), 514–526. https://doi.org/10.3189/002214310792447806, 2010.

520   Cape, M.R., M. Vernet, P. Skvarca, S. Marinsek, T. Scambos, and E. Domack, Foehn winds link climate-driven warming to
ice shelf evolution in Antarctica, J. Geophys. Res. Atmos.,120, 11,037–11,057,doi:10.1002/2015JD023465, 2015.

Datta, R. T., Tedesco, M., Fettweis, X., Agosta, C., Lhermitte, S., Lenaerts, J. T. M., & Wever, N., The effect of Foehn-
induced surface melt on firn evolution over the northeast Antarctic peninsula. Geophysical Research Letters, 46, 3822–3831.
https://doi.org/10.1029/ 2018GL080845, 2019.

525   Davies, B., Hambrey, M. J., Glasser, N. F., Holt, T., Rodes, A., Smellie, J. L., Carrivick, J. L., & Blockley, S., Ice-dammed
lateral lake and epishelf lake insights into Holocene dynamics of Marguerite Trough Ice Stream and George VI Ice Shelf,
Alexander Island, Antarctic Peninsula. Quaternary Science Reviews, 177, 189–
219. https://doi.org/10.1016/j.quascirev.2017.10.016, 2017.

Dell, R., Arnold, N., Willis, I., Banwell, A., Williamson, A., Pritchard, H. and Orr, A., Lateral meltwater transfer across an
530   Antarctic ice shelf, The Cryosphere, 14, 2313–2330, https://doi.org/10.5194/tc-14-2313-2020, 2020.

De Rydt, J., Gudmundsson, G. H., Rott, H., & Bamber, J. L., Modeling the instantaneous response of glaciers after the collapse of the Larsen B Ice Shelf. Geophysical Research Letters, 42 , 5355-5363. doi: https://doi.org/10.1002/2015GL064355, 2015.

Dunmire, D., Lenaerts, J. T. M., Banwell, A. F., Wever, N., Shragge, J., Lhermitte, S., et al. Observations of buried lake
535 drainage on the Antarctic Ice Sheet. Geophysical Research Letters. https://doi.org/10.1029/2020GL087970, 2020.

Elvidge, A.D., Renfrew, I.A., King, J.C., Orr, A. and Lachlan-Cope, T.A., Foehn warming distributions in nonlinear and linear flow regimes: a focus on the Antarctic Peninsula. Quart. J. of the Royal Meteorological Society, 142, 618-631, doi:10.1002/qj.2489, 2016.

Fürst, J. J., Durand, G., Gillet-chaulet, F., Tavard, L., Rankl, M., Braun, M., & Gagliardini, O., The safety band of Antarctic
540 ice shelves. Nature Climate Change, 6, 2014–2017. https://doi.org/10.1038/NCLIMATE2912, 2016.

Gudmundsson, G. H., Paolo, F. S., Adusumilli, S., & Fricker, H. A., Instantaneous Antarctic ice sheet mass loss driven by thinning ice shelves. Geophysical Research Letters, 46, 13,903–13,909. https://doi.org/10.1029/2019GL085027, 2019.

Hambrey, M. J. et al. Structure and sedimentology of George VI Ice Shelf, Antarctic Peninsula: implications for ice-sheet dynamics and landform development. J. Geol. Soc. 172, 599–613, 2015.

545 Haran, T., J. Bohlander, T. Scambos, T. Painter, and M. Fahnestock. 2014. MODIS Mosaic of Antarctica 2008-2009 (MOA2009) Image Map. [Antarctic Peninsula], Boulder, Colorado USA: National Snow and Ice Data Center. http://dx.doi.org/10.7265/N5KP8037.

Holland, P. R., Jenkins, A., and Holland, D. M., Ice and ocean processes in the Bellingshausen Sea, Antarctica, Journal of Geophysical Research, 115, C05020, doi:10.1029/2008JC005219, 2010.

550 Holland, P. R., Corr, H. F. J., Pritchard, H. D., Vaughan, D. G., Arthern, R. J., Jenkins, A., and Tedesco, M.,The air content of Larsen Ice Shelf, Geophys. Res. Lett., 38, L10 503+, https://doi.org/10.1029/2011gl047245, 2011.

Holt, T.O., Glasser, N.F., Quincey, D. and Siegfried, M.R., Speedup and fracturing of George VI Ice Shelf, Antarctic Peninsula. The Cryosphere, 7: 797-816, 2013.

Kingslake, J., Ely, J. C., Das, I., & Bell, R. E., Widespread movement of meltwater onto and across Antarctic ice shelves.
555 Nature, 544, 349-352. https://doi.org/10.1038/nature22049, 2017.

King, J. C., Bannister, D., Hosking, J. S. and Colwell, S. R., Causes of the Antarctic region record high temperature at Signy Island, 30th January 1982, Atmos. Sci. Lett, 18, 491-496, https://doi.org/10.1002/asl.793, 2017.

Kuipers Munneke, P., Ligtenberg, S. R. M., Van Den Broeke, M. R., & Vaughan, D. G., Firn air depletion as a precursor of Antarctic ice-shelf collapse. Journal of Glaciology, 60(220), 205–214. https://doi.org/10.3189/2014JoG13J183, 2014.

560 LaBarbera, C. H. and MacAyeal, D. R.,Traveling supraglacial lakes on George VI Ice Shelf, Antarctica, Geophysical Research Letters, 38, L24501, doi:10.1029/2011gl049970, 2011.

Ching-Yao Lai, Jonathan Kingslake, Martin G. Wearing, Po-Hsuan Cameron Chen, Pierre Gentine, Harold Li, Julian J. Spergel, J. Melchior van Wessem., Vulnerability of Antarctica's ice shelves to meltwater-driven fracture. Nature, 584 (7822): 574 doi: 10.1038/s41586-020-2627-8, 2020.

565 Leduc-Leballeur, M., Picard, G., MacElloni, G., Mialon, A., & Kerr, Y. H., Melt in Antarctica derived from Soil Moisture and Ocean Salinity (SMOS) observations at L band. Cryosphere, 14(2), 539–548. https://doi.org/10.5194/tc-14-539-2020, 2020.

Leeson, A., Forster, E., Gourmelen, N., & van Wessem, J. M., Evolution of supraglacial lakes on the Larsen B ice shelf in the decades before it collapsed. Geophysical Research Letters, 47. doi: https://doi.org/10.1029/ 2019GL085591, 2020.

570 Lenaerts, J. T. M., Lhermitte, S., Drews, R., Ligtenberg, S. R. M., Berger, S., Helm, V., et al. Meltwater produced by wind–albedo interaction stored in an East Antarctic ice shelf. Nature Climate Change, 7, 58-63. doi: https://doi.org/10.1038/NCLIMATE3180, 2017.

Lhermitte et al., Damage accelerates ice shelf instability and mass loss in Amundsen Sea Embayment, PNAS, https://doi.org/10.1073/pnas.1912890117, 2020.

575 Lindsley, R.D. and Long, D. G, Enhanced-Resolution Reconstruction of ASCAT Backscatter Measurements, IEEE Transactions on Geoscience and Remote Sensing, 54, 5, 2589-2601, doi: 10.1109/TGRS.2015.2503762, 2016.

Luckman A, Elvidge A, Jansen D, Kulessa B, Kuipers Munneke P, King J and Barrand NE., Surface melt and ponding on Larsen C Ice Shelf and the impact of föhn winds. Antarct. Sci. 26(06), 625–635. doi:10.1017/S0954102014000339, 2014.

MacAyeal DR, Scambos TA, Hulbe CL and Fahnestock MA., Catastrophic ice-shelf break-up by an ice-shelf-fragment-580 capsize mechanism. J. Glaciol. 49(164), 22–36, 2003.

Magand, O., Picard, G., Brucker, L., Fily, M., & Genthon, C., Snow melting bias in microwave mapping of Antarctic snow accumulation. The Cryosphere, 2(2), 109 - 115. www.the-cryosphere.net/2/109/2008/, 2008.

Moussavi, M.S., Pope, A., Halberstadt, A. R. W. Trusel, L. D. Cioffi, L. & Abdalati, W., Antarctic Supraglacial Lake Detection Using Landsat 8 and Sentinel-2 Imagery: Towards Continental Generation of Lake Volumes, Remote Sensing 12, 585 134; doi:10.3390/rs12010134, 2020.

Moussavi, M.S., Abdalati, W., Pope, A., Scambos, T., Tedesco, M., MacFerrin, M., and Grigsby, S., Derivation and validation of supraglacial lake volumes on the Greenland Ice Sheet from high-resolution satellite imagery. Remote Sensing of Environment 183: 294-303. doi:10.1016/j.rse.2016.05.024, 2016.

Paolo, F. S., Fricker, H. A., & Padman, L., Volume loss from Antarctic ice shelves is accelerating. Science, 348, 327–331. 590 https://doi.org/10.1126/science.aaa0940, 2015.

Pearson, M. R. and Rose, I. H.: The dynamics of George VI Ice Shelf, British Antarctic Survey Bulletin, 52, 205–220, 1983.

Picard, G., & Fily, M., Surface melting observations in Antarctica by microwave radiometers: Correcting 26-year time series from changes in acquisition hours. Remote Sensing of Environment, 104(3), 325–336. https://doi.org/10.1016/j.rse.2006.05.010, 2006.

595 Picard, G., Fily, M., & Gallee, H., Surface melting derived from microwave radiometers: a climatic indicator in Antarctica. Annals of Glaciology, 46(2002), 29–34. https://doi.org/10.3189/172756407782871684, 2007.

Philpot, WD.,Bathymetric mapping with passive multispectral imagery, Applied Optics, 28(8): 1569–1577, https://doi.org/10.1364/AO.28.001569, 1989.

Pope, A., Scambos, T. A., Moussavi, M., Tedesco, M., Willis, M., Shean, D., and Grigsby, S.: Estimating supraglacial lake 600 depth in West Greenland using Landsat 8 and comparison with other multispectral methods, The Cryosphere, 10, 15–27, https://doi.org/10.5194/tc-10-15-2016, 2016.

Pritchard, H. D., Ligtenberg, S. R. M., Fricker, H. A., Vaughan, D. G., van den Broeke, M. R., and Padman, L., Antarctic ice-sheet loss driven by basal melting of ice shelves, Nature, 484, 502–505, 10.1038/nature10968, 2012.

22

Readinger, C., Operational Antarctic Ice Front and Coastline Data Set (2019-2020), U. S. National Ice Center, 2020.

605   Reynolds, J. M. and Hambrey, M. J., The structural glaciology of George VI Ice Shelf, Antarctic Peninsula, British Antarctic Survey Bulletin, 79, 79–95, 1988.

Reynolds, J.M., Lakes on George VI Ice Shelf, Antarctica. Polar Record, 20, 425–432, 1981.

Rignot, E., Jacobs, S., Mouginot, J. & Scheuchl, B. Ice Shelf Melting Around Antarctica. Science, 2013.

Rignot, E., Mouginot, J., Scheuchl, B., van den Broeke, M., van Wessem, M. J., & Morlighem, M., Four decades of
610   Antarctic Ice Sheet mass balance from 1979–2017. Proceedings of the National Academy of Sciences of the United States of America, 116(4), 1095– 1103. https://doi.org/10.1073/pnas.1812883116, 2019.

Robel, A. A., & Banwell, A. F., A speed limit on ice shelf collapse through hydrofracture. Geophysical Research Letters, 46, 12092-12100. doi: doi:10.1029/2019gl084397, 2019.

Scambos, T. A., Hulbe, C., Fahnestock, M. & Bohlander, J., The link between climate warming and break-up of ice shelves
615   in the Antarctic Peninsula. Journal of Glaciology 46, 516–530, 2000.

Scambos, T., Hulbe, C., & Fahnestock, M., Climate-induced ice shelf disintegration in the antarctic peninsula, Antarctic Peninsula climate variability: Historical and paleoenvironmental perspectives, Vol. 79, 79–92, Washington, DC: American Geophysical Union. Antarct Res. Ser., 2003.

Scambos, T., Bohlander, J., Schuman, C., & Skvarca, P., Glacier acceleration and thinning after ice shelf collapse in the
620   Larsen B embayment, Antarctica. Geophysical Research Letters, 731. doi: https://doi.org/10.1029/ 2004GL020670, 2009.

Scambos, T., Fricker, H. A., Liu, C.-C., Bohlander, J., Fastook, J., Sargent, A., et al., Ice shelf disintegration by plate bending and hydro-fracture: satellite observations and model results of the 2008 Wilkins ice shelf break-ups. Earth Planetary Science Letters, 280, 51-60. doi: https://doi.org/10.1016/ j.epsl.2008.12.027, 2009.

Siegert, M., Atkinson, A., Banwell, A., Brandon, M., Convey, P., Davies, B., et al., The Antarctic Peninsula Under a 1.5°C
625   Global Warming Scenario. Frontiers in Environmental Science. doi: https://doi.org/10.3389/ fenvs.2019.00102, 2019.

Shepherd, A., Ivins, E., Rignot, E., Smith, B., Van den broeke, M., Velicogna, I., Whitehouse, P ., Briggs, K., Joughin, I. & Krinner, G., Mass balance of the Antarctic Ice Sheet from 1992 to 2017. Nature, 558, 219-222, 2018.

Smith, J.A., Bentley, M.J., Hodgson, D.A., Cook, A.J., George VI Ice Shelf: past history, present behaviour and potential mechanisms for future collapse. Antarct. Sci. 19, 131e142, 2007.

630   Smith, B. et al., Pervasive ice sheet mass loss reflects competing ocean and atmospheric processes, Science 10.1126/science.aaz5845, 2020.

Sneed WA and Hamilton GS., Evolution of melt pond volume on the surface of the Greenland Ice Sheet. Geophys. Res. Lett., 34(3), L03501, doi: 10.1029/2006GL028697, 2007.

Torinesi, O., Fily, M., & Genthon, C., Variability and trends of the summer melt period of Antarctic ice margins since 1980
635   from microwave sensors. Journal of Climate, 16(7), 1047–1060. https://doi.org/10.1175/1520-0442(2003)016<1047:VATOTS>2.0.CO;2, 2003.

Turner, J., Lu, H., White, I., King, J. C., Phillips, T., Hosking, J. S., Bracegirdle, T. J., Marshall, G. J., Mulvaney, R., and Deb, P., Absence of 21st century warming on Antarctic Peninsula consistent with natural variability, Nature, 535, 411–415, https://doi.org/10.1038/nature18645, 2016.

640   Trusel, L., Frey, K. E., Das, S. B., Karnauskas, K. B., Munnege, P. K., van Meijgaard, E., & van den Broeke, M. R.,
Divergent trajectories of Antarctic surface melt under two twenty-first-century climate scenarios. Nature Geoscience, 8, 927-932. doi: https://doi.org/10.1038/ngeo2563, 2015.

Tuckett, P. A., Ely, J. C., Sole, A. J., Livingstone, S. J., Davidson, B. J., van Wessem, J. M., & Howard, J., Rapid
accelerations of antarctic peninsula outlet glaciers driven by surface melt. Nature Communications, 10. doi:
645   https://doi.org/10.1038/s41467-019-12039-2, 2019.

Van der Veen, C. J., Fracture propagation as means of rapidly transferring surface meltwater to the base of glaciers.
Geophys. Res. Lett., 34(L01501), 2007.

Van Wessem, J. M., Reijmer, C. H., van de Berg, W. J., van den Broeke, M. R., Cook, A. J., van Ulft, L. H., & van
Meijgaard, E.,Temperature and wind climate of the Antarctic peninsula as simulated by a high-resolution regional
650   atmospheric climate model. Journal of Climate, 28, 7306–7326. https://doi.org/10.1175/JCLI-D-15-0060.1, 2015.

Wager, A. C., Flooding of the ice shelf in George VI Sound. British Antarctic Survey Bulletin, No 28, p 71-74, 1972.

Weber Hoen, E, and Zebker, H. A., Penetration depths inferred from interferometric volume decorrelation observed over the
Greenland Ice Sheet," in IEEE Transactions on Geoscience and Remote Sensing, 38, 6, pp. 2571-2583, doi:
10.1109/36.885204, 2020.

655   Wiesenekker, J., Kuipers Munneke, P., van den Broeke, M., & Smeets, C., A multidecadal analysis of Föhn winds over
Larsen C ice shelf from a combination of observations and modeling. Atmosphere, 9(5), 172.
https://doi.org/10.3390/atmos9050172, 2018.

Wille, J. D., Favier, V., Dufour, A., Gorodetskaya, I. V., Turner, J., Agosta, C., & Codron, F., West Antarctic surface melt
triggered by atmospheric rivers. Nature Geoscience, 12(11), 911–916. https://doi.org/10.1038/s41561-019-0460-1, 2019.

660   Williamson, A. G., Banwell, A. F., Willis, I. C., and Arnold, N. S., Dual-satellite (Sentinel-2 and Landsat 8) remote sensing
of supraglacial lakes in Greenland, The Cryosphere, 12, 3045–3065, https://doi.org/10.5194/tc-12-3045-2018, 2018.